Noname manuscript No.
(will be inserted by the editor)

Level set topology optimisation of synchronous reluctance machines using a body-fitted mesh representation

Erin Kuci · Miche Jansen · Olivier Coulaud

Received: date / Accepted: date

Abstract This paper presents a framework for the topology optimization of electro-mechanical design problems. While the design is parametrized by means of a level set function defined on a fixed mesh of the design domain, mesh adaptation is used to generate a second mesh that conforms to the domain delineated by the iso-zero of the level set function. This body-fitted mesh is used in the finite element simulation of the physical problem in order to accurately represent the electro-magnetic interface phenomena. An appropriate combination of the two geometry representations is obtained through the velocity field to ensure a consistent design space as the topology optimisation process unfolds. The method is applied to the joint electro-mechanical optimisation of a synchronous reluctance machine (SynRM).

Keywords Topology optimisation · Body-fitted mesh · Lie derivative · Synchronous reluctance machine · Nonlinear programming

1 Introduction

Synchronous reluctance machines are electro-mechanical energy converters which transform electric energy into mechanical energy. Despite their early invention by Kostko in 1923 [43], they did not find widespread use as motors until the late 1970s because of the complexity of the power electronics control they require. Due to their robustness and efficiency over a wide range of speeds, they are an interesting alternative to traditional induction and permanent magnet machines in various applications, including hybrid and electric vehicles as well as traction applications [21, 13, 29]. A SynRM consists of a fixed part, called the stator, with windings fed by a sinusoidal current, and a rotating part, called the rotor, with flux barriers (see Fig. 1).

Several multiphysics approaches have been proposed over the last decade to achieve electrical machine designs with high electromagnetic performances, meeting requirements on the rotor

This work was supported in part by the Walloon Region of Belgium under grant PIT 7706 Traction2020. The present research benefited from computational resources made available on the Tier-1 supercomputer of the Fédération Wallonie-Bruxelles, infrastructure funded by the Walloon Region under the grant agreement no 1117545.

E. Kuci · M. Jansen · O. Coulaud
Centre de recherche en aéronautique (Cenaero)
Rue des Frères Wright 29, 6041 Gosselies, Belgium
E-mail: {erin.kuci, miche.jansen, olivier.coulaud}@cenaero.be

integrity [49, 16], as well as the assembly process [8, 45] and ensuring lifelong reliability, see for instance [62, 8], or more recently [22, 23, 55]. These industrial design issues have been handled by applying shape optimisation [15, 53, 48] on two-dimensional and three-dimensional multiphysics models to find out the optimal layout of their underlying CAD description. However, the initial choice of design variables among the CAD parameters, inherent to the method, may limit the ability of this approach to bring innovative layouts that would lead to better performances. There is therefore a desire to move towards topology optimisation for its ability to generate innovative geometrical layouts, regardless of the design parameterization, as long as it does not compromise the accuracy of such models.

Topology optimisation has been an active research area since the seminal work of Bendsøe and Kikuchi in the late 1980s [9], as reviewed in a number of papers, [20, 24, 57]. Two main paths have been followed to reduce the complexity of representing topological changes with a classical CAD based shape optimisation and make this method available for industrial designs: the density-based approach [10] and the level set approach [54, 7, 66]. Whereas the most prominent density-based approach represents the geometry by the presence or absence of material at each point of the design domain, the level set approach represents the geometry implicitly by the zero level set of a scalar function. Both geometrical representations, which allow to easily handle large shape modifications, or merging geometric entities such as holes, without degenerating the model, have been first applied successfully to structural optimisation, see [7, 66], but also in electromagnetic design of electrical rotating machines and inverse problems, see for instance [46, 39, 18]. In more advanced level set approaches, holes, can be created if the method is combined with a topological derivative (see for instance [52, 36, 30, 26, 67] or [58] for more theoretical aspects), or more recently, it is combined with the density approach [65, 31].

The level set optimisation can be performed on a fixed mesh by adopting intermediate volume densities to modify the behaviour of the elements cut by the iso-zero, in a similar way to the density-based approach [66]. However, this approach leads to blurred boundaries which can cause numerical convergence issues in electromagnetic problems (with eventually localized boundary effects) and many other cases, such as fluid flow problems and structural problems with design-dependent loadings. Several immersed boundary techniques [63, 33] and the extended finite element method (XFEM) [50, 42, 64, 51] have therefore been proposed to represent the sharp boundary in the physical model and obtain an accurate response along the interface while

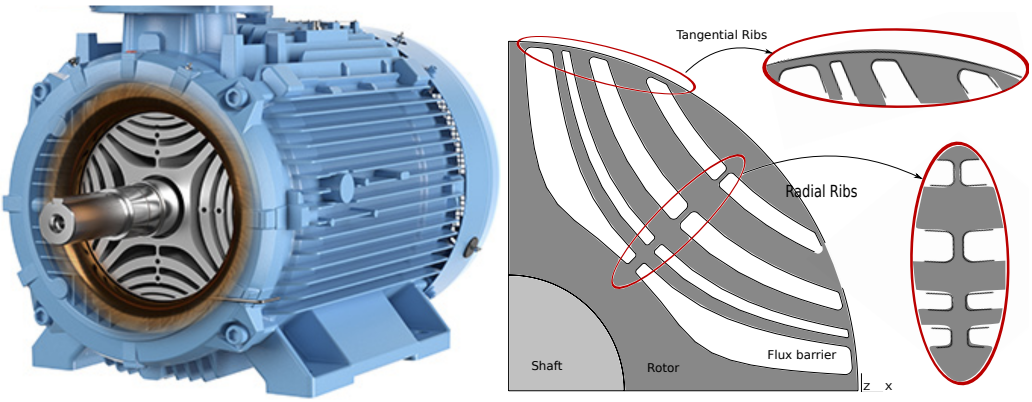

Fig. 1: A synchronous reluctance machine (SynRM) from ABB Motors and a representative lamination of a rotor with flux-barriers, including radial as well as tangential iron bridges (see [45]).

avoiding remeshing. However, XFEM makes it difficult to use existing numerical solvers, mostly based on FEM, which limits the extension of topology optimisation to such complex systems.

An alternative level set topology optimisation method using body-fitted mesh discretization has been successfully applied to electromagnetic waveguides with localized boundary effects [70, 69], structural problems [3, 34, 5, 6, 68], and more recently, heat exchangers [27], for which the accuracy of the physical response in the vicinity of the boundaries is a major concern. The ability of this method to use the FEM solver as it is, i.e. without requiring any modification of the physical equations, regardless of the physics, along with the simplified handling of manufacturability constraints [42] make it a valuable alternative to the classical approaches.

In all cases, a gradient-based algorithm solves the large scale topology optimisation problem as it leads to fewer simulations of the underlying PDE model compared to a gradient-free algorithm. A substantial gain in computation time is furthermore obtained when the derivatives of the performance functions with respect to the level set design variables are obtained analytically instead of evaluating a finite difference, which requires one additional solution of the physical problem for each design variable. The variation of the residual with respect to a level set that brings modifications in the boundaries of the system requires terms to account for the implicit dependency of the residual in the continuous flow of geometrical modification, see [59, 41].

Shape sensitivities have been obtained in the past through the velocity method, [59]. This approach uses the variation of the shape design variable as the parameter describing a smooth geometrical transformation of the domain, with no tearing nor overlapping, that brings the boundaries of the domain from their unperturbed position to their perturbed position. The variation of the parameter determines therefore a flow characterized by a velocity field, which has been applied successfully to elasticity problems where the components of the solution of the physical problem are scalar fields, see for instance [72]. Following this approach, analytical formulas have also been proposed in other disciplines such as electromagnetics, based on classical vector analysis, as in [56, 11]. The complex behaviour of a vector field under the transformation that brings a modification of the system boundaries has been handled with the Lie derivative, [38, 37]. These material derivatives have been used more recently by [40] in order to overcome the limitations of the vector analysis approach, classically used for the scalar field. This approach has been applied to the sensitivity calculation of a linear acoustic and electromagnetic boundary integral problems [41]. We have shown in [44] that using the Lie derivative, sensitivities for more complex problems (non linear electromagnetic and elastic) can be efficiently computed in both 2D and 3D thanks to a velocity field based on the parametrization of the geometric model of the domain. On a practical level, this approach is very efficient since it limits the support of the volume integrals involved in the sensitivity formulas to a one-layer-thick layer of finite elements on both sides of the surfaces involved in the shape variation.

In this paper, we propose to tackle the level set topology optimisation by the Method of Moving Asymptotes (MMA) [60] using body-fitted mesh discretization and adjoint shape sensitivity formulation. The sensitivities are computed analytically based on the Lie derivative from previous work [44] with a velocity field adapted to the level set method. The paper is organized as follows. The geometry description is discussed in Section 2 and the general optimisation problem is posed in Section 3. Section 4 deals with the sensitivities associated with the level set shape modifications and provide analytic formulas to evaluate them practically. In Sections 5, the level set topology optimisation with body-fitted spatial discretization is applied to the joint torque ripple and von Mises stress minimization of a synchronous reluctance machine.

2 Geometry description using body-fitted spatial discretization

We model the geometry of the SynRM as a bounded domain Ω consisting of two materials (steel and air) distributed in domains Ω_1 and Ω_2 respectively, with no overlapping, i.e. $\Omega_1 \cap \Omega_2 = \emptyset$ and separated by the interface $\partial\Omega_{12}$. The material distribution is described by means of a level set function ϕ,

$$\begin{cases} \phi(\boldsymbol{x}) < 0 & \forall \boldsymbol{x} \in \Omega_1, \\ \phi(\boldsymbol{x}) = 0 & \forall \boldsymbol{x} \in \partial\Omega_{12}, \\ \phi(\boldsymbol{x}) > 0 & \forall \boldsymbol{x} \in \Omega_2, \end{cases} \tag{1}$$

at a given point $\boldsymbol{x}$ of Ω, see Fig. 2.

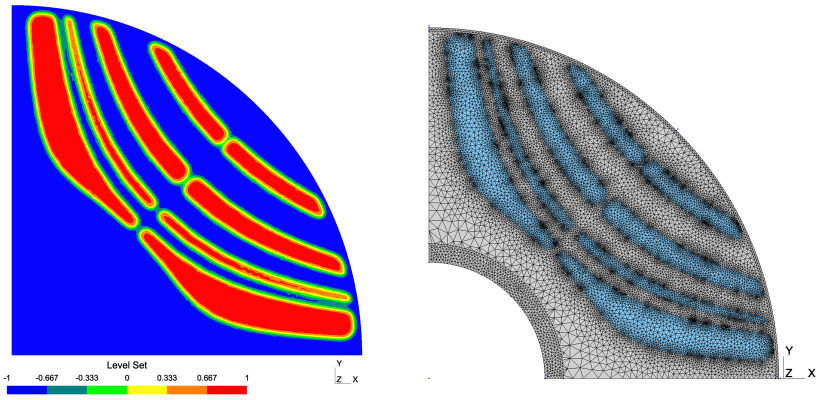

Fig. 2: A level set function of a representative SynRM rotor (left) and the body-fitted computational mesh (right), i.e. conformal to the boundaries of the level set, are considered.

Most state-of-the-art methods of level set based topology optimisation consider a fixed grid for analysis, either by using a dedicated SIMP-like approach, which alters the equations of the physical problem at hand, or an immersed-boundary technique (such as XFEM) so as to preserve the quality of the physical solutions. Alternatively, in this work, the modified geometries obtained by the variations of the level set function are discretized spatially by conformal meshes which make each phase (Ω_1 and Ω_2) readily available for accurate FEM analysis.

We consider throughout this paper a triangular mesh of Ω, denoted $\mathcal{H}$, as well as a nodal valued level set field ϕ. A number of methods for obtaining a conformal mesh $\mathcal{H}^c$, i.e. which can be divided into the two sub-meshes $\mathcal{H}_{\Omega_1}$ and $\mathcal{H}_{\Omega_2}$, such that $\mathcal{H}^c = \mathcal{H}_{\Omega_1} \cup \mathcal{H}_{\Omega_2}$, have been developed over the years. In the most successful approaches, the original boundary $\partial\Omega_{12}$ is first smoothed, then the mesh is made conformal to this approximated interface, see for instance [19] and more recently [28]. In our approach, the level set function is represented by a field defined on a finer background mesh, called $\mathcal{H}_\phi$, which can thus be interpolated on any other mesh and in particular on $\mathcal{H}$, as shown in the figure 3.

While the vertices of $\mathcal{H}$ can be moved directly onto $\partial\Omega_{12}$, [70, 69], this operation may result in a poor boundary representation, especially when the mesh is not sufficiently refined where the boundary has a high curvature. With the aim of alleviating this issue, we propose a prior mesh adaptation so as to ensure that cutting the mesh along the level set iso-zero leads to an accurate representation of $\partial\Omega_{12}$. In particular, on the contrary to [70] where the number of

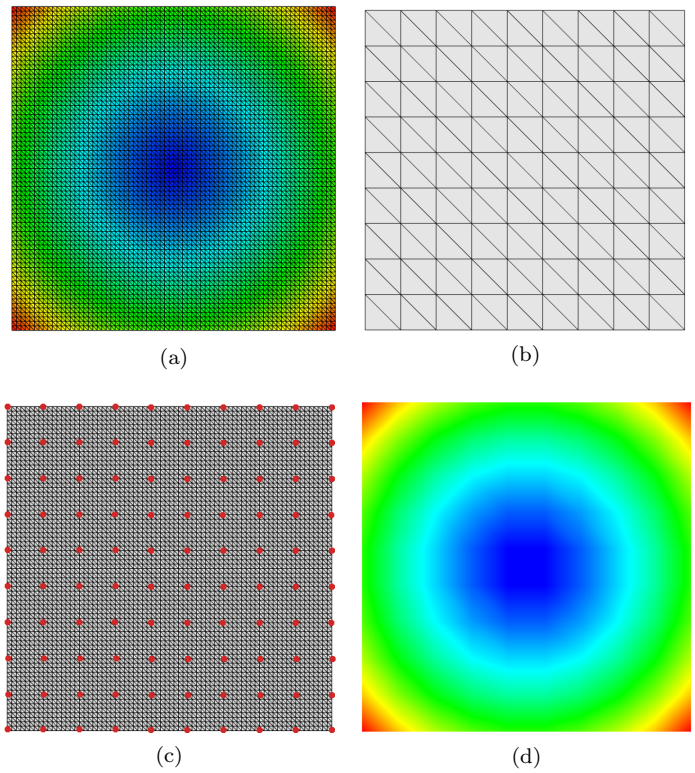

Fig. 3: The level set function is defined at the nodes of a refined background mesh $\mathcal{H}_\phi$ 3a. When the level-set values have to be computed on another mesh $\mathcal{H}$ 3b, its vertices are located into $\mathcal{H}_\phi$ 3c and a linear interpolation leads to a nodal representation on $\mathcal{H}$ 3d.

vertices and elements of the mesh is fixed, this later step allows to modify the complexity of the initial mesh, and to add elements if the shape of the iso-zero requires a finer discretization. Once this adaptation step is achieved, the vertices of the resulting mesh are moved along the level set iso-zero. Additional steps may sometimes be required as this method may break the validity of the mesh, e.g. by cutting edges crossing the iso-zero level set ($\phi \equiv 0$), as reported in [5]. Afterwards, a second mesh adaptation is performed in order to improve the overall mesh quality. This last mesh adaptation replaces the Laplacian smoothing of [70, 69]. All the steps of our methodology are further described in the next sections and are illustrated for a radial level function, on a square domain, see Fig. 4. We implemented this approach in the open source library MAdLib [1] as part of this work.

2.1 Conforming mesh to the level set boundary

In order to make the mesh conformal to the level set, an edge-based mesh modification is performed. This corresponds to the step between 4b and 4c of Fig. 4, and it is also deeply used to go from 4a to 4b. Assuming that the values of ϕ are known at the vertices of $\mathcal{H}$ (which in practice are interpolated linearly from the background mesh $\mathcal{H}_\phi$), we move the vertices of each edge crossed by the iso-zero of the level set to the position where ϕ vanishes. Letting e be one of

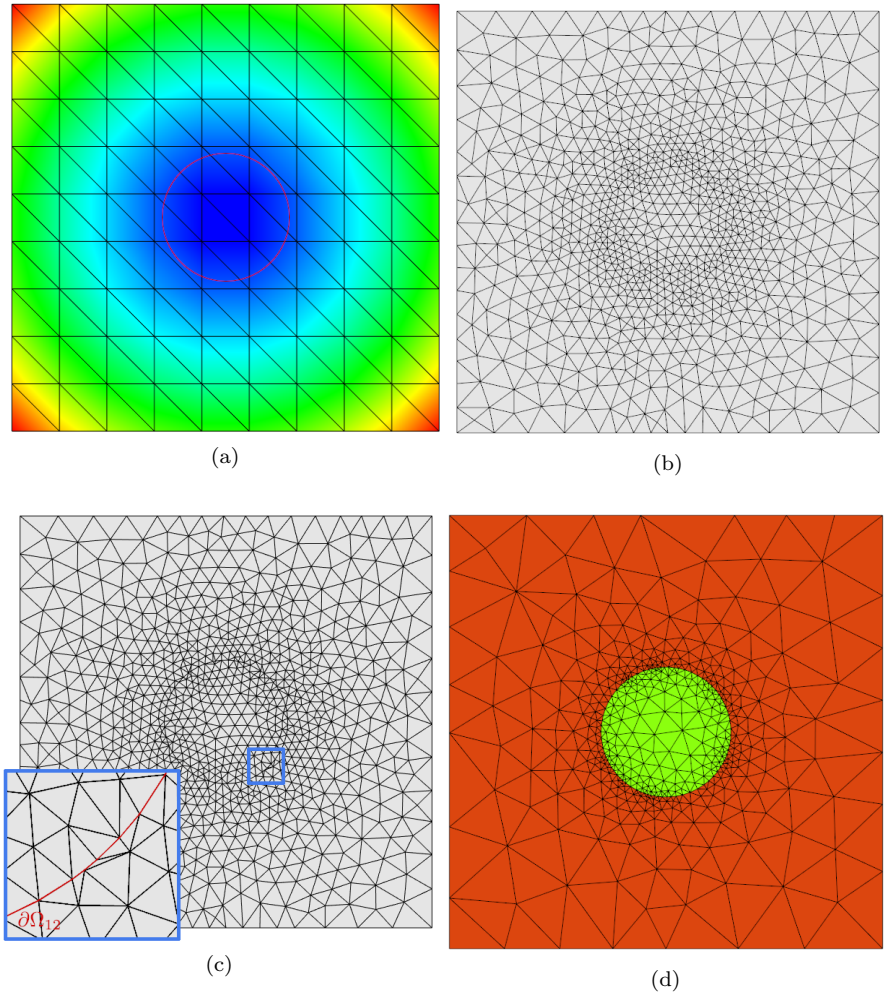

Fig. 4: A representative level set based mesh adaptation process for a radial level set function. The initial mesh $\mathcal{H}$ (4a with the iso-zero in red) is first further refined in regions where $\partial\Omega_{12}$ is highly curved, resulting in a level-set based adapted mesh $\mathcal{H}^*$ 4b. The mesh vertices are then moved to the iso-zero of the level set, giving a low-quality conform mesh $\mathcal{H}^c_{low}$ (4c with a zoom on the blue squared area and the iso-zero in red). Finally, in order to a obtain a conform mesh $\mathcal{H}^c$ with reasonable qualities, the discretization of the boundary $\partial\Omega_{12}$ is fixed and a last mesh adaptation is performed, improving the elements qualities 4d. At the very end, a mesh classification is done, defining whether each triangle belongs to either Ω_1 or Ω_2.

these edges defined by two vertices, respectively x_1 and x_2, such that $\phi(x_1) > 0$ and $\phi(x_2) < 0$, we obtain the point

$$x_\phi = \frac{\phi(x_1)x_2 - \phi(x_2)x_1}{\phi(x_1) - \phi(x_2)}, \tag{2}$$

which lies on e and satisfies $\phi(x_\phi) = 0$. The most obvious approach would consist in splitting the edge at the location x_ϕ using a standard mesh split operator, see Fig 5. Unfortunately, this

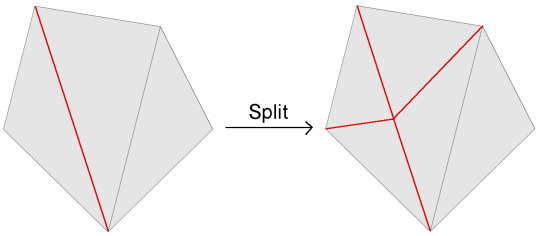

Fig. 5: The 2D edge split operator. The red edge of the left mesh is split (in this example, in the middle), leading to the right mesh, which has got an additional vertex and four new edges (in red).

usually leads to a poor mesh quality, or at least some edges of $\partial\Omega_{12}$ would remain very short. Instead, moving one of the two vertices of e at the location x_ϕ leads to much better results. Following this idea, between x_1 and x_2, the closest point to x_ϕ is moved while keeping the mesh connectivity unchanged. If the operation is not allowed because the mesh validity is broken, another try is done with the other vertex. Finally, in the rare case that neither of the vertices can be moved, the edge is split, as shown in Fig. 5. An example of such a mesh modification, obtained by only changing the vertices locations, is illustrated in Fig. 6. At this step, neither

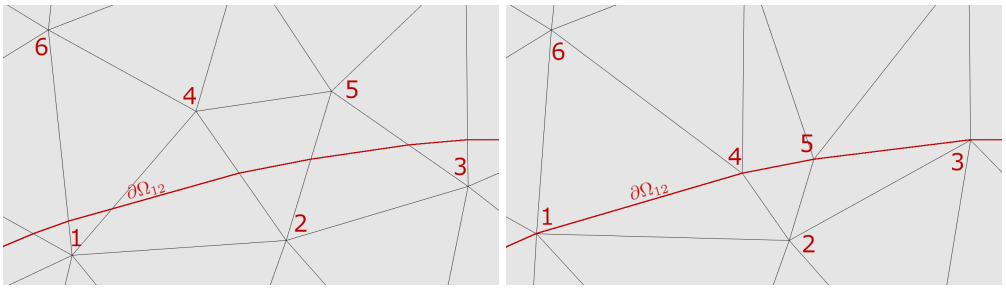

Fig. 6: Mapping of the vertices of a mesh (left) to the closest point crossed by the iso-zero of the level set (red line). The body-fitted mesh (right) is obtained by moving the vertices 1, 3, 4 and 5. Once the vertices are moved, the level set is aligned with mesh edges.

the accuracy of $\partial\Omega_{12}$ boundary representation, nor the quality of the mesh elements are taken into account. In order to get a better approximation of $\partial\Omega_{12}$, an a-priori mesh adaptation is performed before conforming the mesh to the level set, as described in next section.

2.2 An a-priori level set based mesh adaptation

As described in subsection 2.1, simply fitting the mesh to the interface $\partial\Omega_{12}$ does not ensure that $\partial\Omega_{12}$ is discretized accurately enough. Therefore, the mesh is first refined in the regions where the interface makes large variations by means of a size-field mesh adaptation, then the vertices are moved to match $\partial\Omega_{12}$, thus leading to an accurate discretizations of the boundary. Letting $\{x_1, ..., x_i, ..., x_k\}$ be the set of vertices of $\mathcal{H}$, the size-field based mesh adaptation lies in the definition of the target sizes $\{h_1, ..., h_i, ..., h_k\}$ based on the neighboring edges of each vertex x_i. Then, the automatic mesh adaptation procedure of MAdLib modifies the mesh so that the

edges in a neighborhood of x_i have a length close (up to a tolerance) to h_i, see Fig. 7. The mesh adaptation problem is reduced to the definition of suitable reference (target) sizes.

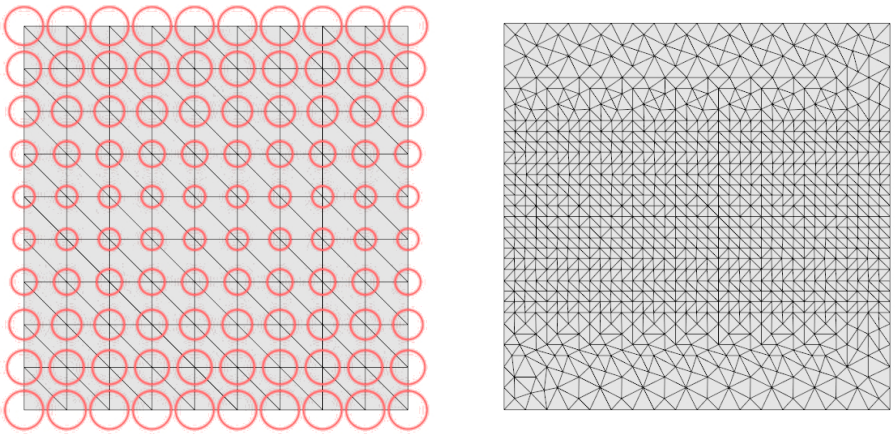

Fig. 7: A size-field based adaptation of an initial mesh (left) with the size-field unit balls (red) leads to the adapted mesh (right).

In our case, the way the sizes are computed differs between the vertices which lie on $\partial\Omega_{12}$ and the other ones. At the beginning of the process, the mesh $\mathcal{H}$ does not fit the iso-zero of the level set, that is why the method described by the subsection 2.1 is first applied, giving a body fitted mesh $\mathcal{H}^c$. Then, for each boundary vertex x_b belonging to $\partial\Omega_{12}$, a reference size $h_b > 0$ is defined, which depends on the curvature of $\partial\Omega_{12}$ at that point. Indeed, as illustrated by Fig. 8, the size h_b is built through a distance $d \geq 0$, which measures the gap between $\partial\Omega_{12}$ and a straight line. Assuming that the level set does not have non-manifold configurations, x_b is surrounded by two edges (e_b^1, e_b^2) which belong to $\partial\Omega_{12}$. These edges can be used to define a unit normal vector $\boldsymbol{n}$ to $\partial\Omega_{12}$, see Fig. 8. Likewise, the unit vector $\boldsymbol{u} = \frac{e_b^1}{|e_b^1|_2}$ is defined, with $|.|_2$ being the 2D Euclidean norm. Then, the Euclidean scalar product $d = |(\boldsymbol{n}, \boldsymbol{u})_2|$ provides a measure of the distance between $\partial\Omega_{12}$ and its tangent line at the vertex x_b. Since $\boldsymbol{n}$ and $\boldsymbol{u}$ are both unit vectors, it implies that $d \in [0, 1)$, where $d = 0$ corresponds to the case in which $\partial\Omega_{12}$ is a straight line. The reference size h_b is obtained by interpolating between a minimal length $h_{min} > 0$ and a maximal length $h_{max} > 0$:

$$h_b = (1 - d^\alpha)h_{max} + d^\alpha\, h_{min}, \tag{3}$$

where $\alpha > 0$ is a positive parameter giving the sensitivity of h_b with respect to d. While other choices of α might lead to suitable results as well, a fixed $\alpha = 1/100$ is used in this work. By doing so, if $\partial\Omega_{12}$ is a straight line at x_b, then $h_b = h_{max}$. On the contrary, h_b gets closer to h_{min} as the angle made by $\partial\Omega_{12}$ at x_b increases.

Finally, we define a reference length for the vertices that do not belong to $\partial\Omega_{12}$. This is done in two steps. First, we define the reference length to be h_{max} and then the size-field is smoothed over the whole mesh, diffusing the small lengths of $\partial\Omega_{12}$ to the other vertices. More precisely, the smoothing step is based on the following principle. For each vertex of the mesh x_i with initial length h_i, we compute a diffused length over all the mesh, which is obtained by increasing the length with the distance to x_i. This way, the diffused length h_j^i is defined for all $\mathbf{x}_j, j \neq i$ at the

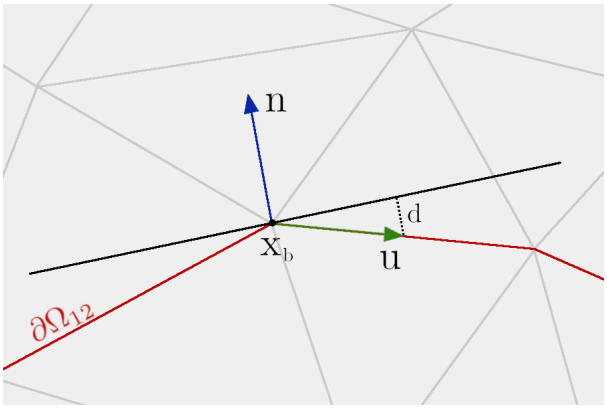

Fig. 8: A representative boundary vertex $x_b \in \partial\Omega_{12}$, its unit normal vector $\boldsymbol{n}$ to $\partial\Omega_{12}$ and the unit vector $\boldsymbol{u}$, given by one of the normalized boundary edges surrounding x_b, (in red). The reference length h_b depends on the normalized distance between $\partial\Omega_{12}$ and its tangent line, given by $d = |(\boldsymbol{n}, \boldsymbol{u})_2|$.

location of x_j. If $h_j^i < h_j$, then h_j is replaced by h_j^i. The more general anisotropic case, and in particular the way the reference lengths are diffused, is described in Ref. [4]. Notice that this smoothing depends on a parameter $\beta > 1$, which controls the magnitude at which the lengths are increased with respect to the distance, see Fig. 9. Once the reference lengths $\{h_1, ..., h_k\}$ are

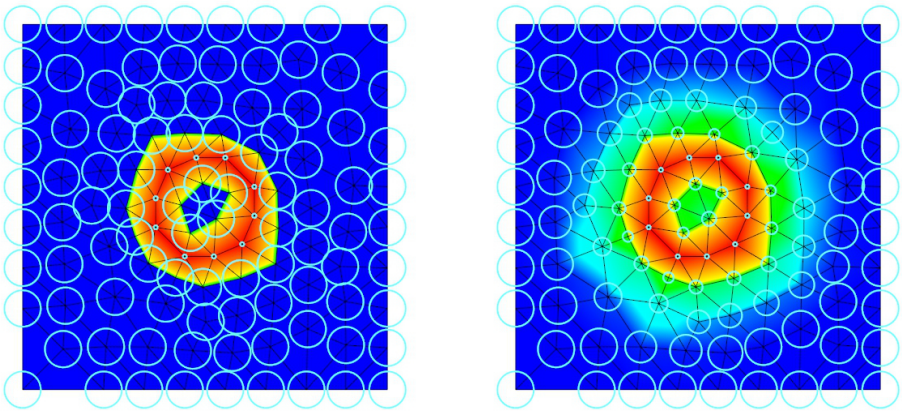

Fig. 9: Reference length definition for a circular level set. Left: the map and the unit balls of the curvature-based size-field without smoothing. Right: the same map and unit balls with a length smoothing.

computed for the vertices $\{x_1, ..., x_k\}$ of $\mathcal{H}_\Omega$, they are normalised, in order to achieve a given mesh complexity N. More precisely, let $h : \Omega \to (0, +\infty)$ denotes the $\mathbb{P}_1$ map of $\{h_1, ..., h_k\}$ onto

$\mathcal{H}_\Omega$. Then, the complexity of h is given by

$$\mathcal{C}(h) = \int_\Omega \frac{1}{h^2(x)} dx. \tag{4}$$

This quantity is the size-field equivalent of the mesh complexity. Indeed, if h is small, then N would be large. Likewise, if h is small, a mesh adaptation with respect to the size-field would produce a large number of elements. In practice, the normalisation step corresponds to replacing h_i, $i = 1, ..., k$ by

$$h_i^N = \left(\frac{1}{N} \int_\Omega \frac{1}{h^2(x)} dx \right)^{\frac{1}{2}} h_i. \tag{5}$$

Finally, once the size-field $\{h_1^N, ..., h_k^N\}$ is computed for all the vertices, $\mathcal{H}^c$ is adapted using MAdLib, resulting in a mesh $\mathcal{H}^*$ that is refined where $\partial\Omega_{12}$ is highly curved. In order to properly discretize $\partial\Omega_{12}$, this process is done several times, with increasing mesh complexity. In particular, it implies to update the level set at each iteration. This task is done by using the fine background mesh $\mathcal{H}_\phi$, which we use to compute the level set on the adapted meshes. Actually, the a priori mesh adaptation method follows the iterative process described by the algorithm 1.

Algorithm 1: Curvature-based mesh adaptation

Input : Initial mesh $\mathcal{H}$
Background mesh $\mathcal{H}_\phi$
Set of increasing complexities $\{N_1, ..., N_l\}$
Output: Adapted mesh $\mathcal{H}^*$
$\mathcal{H}_0 = \mathcal{H}$
for *i=1,...,l* **do**
  Move the vertices of $\mathcal{H}_{i-1}$ onto the level set $\Rightarrow \mathcal{H}_{i-1}^c$
  Compute the reference sizes at the vertices of $\mathcal{H}_{i-1}^c$
  Normalize the sizes to reach the complexity N_i
  Adapt the mesh $\Rightarrow \mathcal{H}_i$ with complexity N_i
  Using $\mathcal{H}_\phi$, interpolate the values of ϕ at the vertices of $\mathcal{H}_i$
end for
$\mathcal{H}^* = \mathcal{H}_l$

Notice that, at this point, only the accuracy of the representation of $\partial\Omega_{12}$ is considered. Notably, the mesh quality is not involved in this process. The improvement of the mesh quality is the purpose of the next subsection.

2.3 Body-fitted mesh and quality improvement

In this subsection, we assume that the initial mesh $\mathcal{H}$ has been modified into the adapted mesh $\mathcal{H}^*$ using the method of the previous subsection. Notice that $\mathcal{H}^*$ is not body-fitted. In this last step, the aim is to produce a body fitted mesh whose elements qualities are reasonably good. First, the vertices of $\mathcal{H}^*$ are moved so that it fits the level set, following the schedule of the subsection 2.1. According to Fig. 4, it corresponds to the step between 4b and 4c. This conformal mesh, whose elements usually have low qualities, is denoted by $\mathcal{H}_{low}^c$. The quality improvement method presented in this paper, which corresponds to the step between 4c and 4d, relies on a suitable size-field based mesh adaptation, while keeping the edges belonging to $\partial\Omega_{12}$ unchanged. This time, the size field will not depend on the curvature but rather on the lengths of the edges belonging to $\partial\Omega_{12}$. More precisely, for each boundary vertex $x_b \in \mathcal{H}_{low}^c \cap \partial\Omega_{12}$, we define a

reference length $\tilde{h}_b$ which is the minimum length of the edges of $\partial\Omega_{12}$ surrounding x_b. In other words, $\tilde{h}_b$ is given by

$$\tilde{h}_b = \min_{e_b \in \partial\Omega_{12}} |e_b|_2, \tag{6}$$

where e_b denotes an edge surrounding x_b. Similarly to the a priori mesh adaptation, the size-field is then spread to the other vertices by the size-field smoothing. Once this size-field definition has been done, MAdLib adapts the mesh accordingly and finally produces the mesh $\mathcal{H}^c$, which is body fitted with elements of good quality. Notice that the edges belonging to the interface $\partial\Omega_{12}$ are constrained during the adaptation process in order to keep the mesh fitted to the level set iso-zero. The whole mesh adaptation process, which turns the initial mesh $\mathcal{H}$ into the body fitted one $\mathcal{H}^c$, is described by the algorithm 2.

Algorithm 2: Flowchart of the level set based mesh adaptation.

Input : Initial mesh $\mathcal{H}$
Background mesh $\mathcal{H}_\phi$
Set of increasing complexities $\{N_1, ..., N_l\}$
Output: Body fitted mesh $\mathcal{H}^c$
$\mathcal{H}_0 = \mathcal{H}$
for *i=1,...,l* **do**
  Move the vertices of $\mathcal{H}_{i-1}$ onto the level set $\Rightarrow \mathcal{H}^c_{i-1}$
  Compute the reference sizes h at the vertices of $\mathcal{H}^c_{i-1}$
  Normalize the sizes to reach the complexity N_i
  Adapt the mesh $\Rightarrow \mathcal{H}_i$ with complexity N_i
  Using $\mathcal{H}_\phi$, interpolate the values of ϕ at the vertices of $\mathcal{H}_i$
end for
Move the vertices of $\mathcal{H}_l$ onto the level set $\Rightarrow \mathcal{H}^c_{low}$
Compute the reference sizes $\tilde{h}$ at the vertices of $\mathcal{H}^c_{low}$
Adapt the mesh with constrained boundary edges $\Rightarrow \mathcal{H}^c$

3 Optimisation with body-fitted spatial discretization

The SynRM rotor experiences topology modifications, controlled by a set of design variables, τ, which are the nodal values of a level set function, ϕ, at the nodes of the fixed non-conformal mesh of the design domain. We consider a FEM-based optimization and divide the design procedure, for the sake of brevity, in electromagnetic performance and proper mechanical design [12, 8].

The electromagnetic performance of the machine can be evaluated with sufficient accuracy in a quasi-static regime. This means that stator windings are supplied with the prescribed three-phase currents, and the simulation is done for a series of equidistant rotor positions over one pole pitch, as a succession of static computations. The magnetostatic formulation, written at the continuous level by its weak formulation, reads: find $\boldsymbol{A}^\star$ the magnetic vector potential verifying appropriate boundary conditions such that the residual

$$r_m(\tau, \boldsymbol{A}^\star, \bar{\boldsymbol{A}}) = \int_{\Omega(\tau)} \nu(\mathbf{curl}\, \boldsymbol{A}^\star)\, \mathbf{curl}\, \boldsymbol{A}^\star \cdot \mathbf{curl}\, \bar{\boldsymbol{A}} - \boldsymbol{J} \cdot \bar{\boldsymbol{A}}\ \mathrm{d}\Omega = 0, \tag{7}$$

for appropriate test function $\bar{\boldsymbol{A}}$, [14]. In (7), $\boldsymbol{B}^\star = \mathbf{curl}\, \boldsymbol{A}^\star$ is the magnetic flux density, $\boldsymbol{H}(\boldsymbol{B}^\star) = \nu(\mathbf{curl}\, \boldsymbol{A}^\star)\ \mathbf{curl}\, \boldsymbol{A}^\star$ is the magnetic field, with ν the reluctivity depending on $\boldsymbol{B}^\star$ (nonlinear material) and $\boldsymbol{J}$ is the current density. Furthermore, the electromagnetic symmetries are exploited to simulate only a quarter of the machine by means of appropriate periodicity boundary conditions.

On the other hand, the mechanical design is based on a linear elastic behaviour of the rotor subjected to a centrifugal body load with a given frequency. For the sake of rapid prototyping, we consider only a single operating point (speed) rather than a time-consuming fatigue life analysis. The weak formulation of the linear elastic equilibrium equations reads in the solid parts Ω_1: find $\boldsymbol{u}^\star$ the displacement field verifying the appropriate boundary conditions such that

$$r_e\left(\tau, \boldsymbol{u}^\star, \bar{\boldsymbol{u}}\right) = \int_{\Omega_1} \boldsymbol{\sigma}(\boldsymbol{\epsilon}^\star) : \nabla \bar{\boldsymbol{u}} - \boldsymbol{g} \cdot \bar{\boldsymbol{u}}\ \mathrm{d}\Omega = 0, \tag{8}$$

for an appropriate test function $\bar{\boldsymbol{u}}$, see [73]. In (8), $\boldsymbol{\epsilon}^\star = \frac{1}{2}((\nabla \boldsymbol{u}^\star) + (\nabla \boldsymbol{u}^\star)^T)$ is the strain tensor and $\boldsymbol{g}$ is an imposed volume force density. The stress tensor $\boldsymbol{\sigma}$ is a symmetric tensor obtained from the strain tensor by means of a constitutive relationship $\sigma_{ij}(\epsilon_{kl}) = C_{ijkl}\ \epsilon_{kl}$.

The design problem is formulated as a constrained optimization problem that aims to determine the level set design variables, τ, that minimize a cost function $f_0(\tau, \boldsymbol{A}, \boldsymbol{u})$, subjected to m inequalities $f_j(\tau, \boldsymbol{A}, \boldsymbol{u}) \leq 0$, $j = 1, \ldots, m$, ensuring the feasibility of the design:

$$\begin{aligned} \min_{\tau} \quad & f_0(\tau, \boldsymbol{A}^\star, \boldsymbol{u}^\star) \\ s.t. \quad & f_j(\tau, \boldsymbol{A}^\star, \boldsymbol{u}^\star) \leq 0,\ j = 1, \ldots, m \\ & \tau^{min} \leq \tau \leq \tau^{max} \\ & r_m(\tau, \boldsymbol{A}^\star, \bar{\boldsymbol{A}}) = 0,\ \forall \bar{\boldsymbol{A}} \\ & r_e(\tau, \boldsymbol{u}^\star, \bar{\boldsymbol{u}}) = 0,\ \forall \bar{\boldsymbol{u}} \end{aligned} \tag{9}$$

The design space of (9) is also limited by side constraints $\tau^{min} \leq \tau \leq \tau^{max}$.

4 Adjoint-based sensitivity with respect to shape variations

A particular performance function $f(\tau, \boldsymbol{A}, \boldsymbol{u})$ that is separable and explicit in terms of the solution fields $\boldsymbol{A}^\star$ and $\boldsymbol{u}^\star$ is considered:

$$f(\tau, \boldsymbol{A}^\star, \boldsymbol{u}^\star) = f_m(\tau, \boldsymbol{A}^\star) + f_e(\tau, \boldsymbol{u}^\star) \tag{10}$$

which can be written in the form of an integral [1]

$$f_m(\tau, \boldsymbol{A}^\star) = \int_{\Omega(\tau)} F_m(\tau, \boldsymbol{A}^\star)\ \mathrm{d}\Omega \tag{11}$$

evaluated at the solution $\boldsymbol{A}^\star$ of (7) and

$$f_e(\tau, \boldsymbol{u}^\star) = \int_{\Omega(\tau)} F_e(\tau, \boldsymbol{u}^\star)\ \mathrm{d}\Omega \tag{12}$$

evaluated at $\boldsymbol{u}^\star$ of (8) respectively; both of them depending implicitly on the level set design variables. The treatment of any other performance function will be similar.

4.1 Design velocity field

Theoretical formulas to express the derivative of f with respect shape design variables τ have been demonstrated in detail using the Lie derivative in [44], in the context of the family of mappings,

$$p_{\delta\tau} : \Omega(\tau) \subset E^3 \mapsto \Omega(\tau + \delta\tau) \subset E^3, \tag{13}$$

parameterized by the set of design variables τ in the Euclidean space E^3, see [59]. This approach is adopted in this paper for the case of level set design variables. A variation $\delta\tau$ of the design variable brings the interfaces of Ω from their current position to their modified position. A flow with a velocity field denoted by $\mathbf{v}$ is determined on E^3 by varying $\delta\tau$ in the family of mappings (13) in a neighborhood of zero, see [44].

On a practical level, there is some freedom in the definition of the mappings (13), see for instance [17], and, hence in the choice of the velocity $\mathbf{v}$, that represents the shape modification. The mathematical expression of the velocity field is the derivative

$$\mathbf{v} = \frac{\mathrm{d}\mathbf{x}}{\mathrm{d}\tau} \tag{14}$$

of the coordinate vector $\mathbf{x} = (x, y, z)$ of the iso-zero level set nodes with respect to the level set values at the fixed grid nodes, where $\{x, y, z\}$ are coordinates on E^3.

Assuming, for sake of brevity, the two-dimensional case and the iso-zero of the level set to be a line segment that cuts the fixed grid, the coordinates vector of each point $\boldsymbol{A}$ located in this interface,

$$\begin{bmatrix} x \\ y \end{bmatrix} = \begin{bmatrix} 1-\eta & 0 & \eta & 0 \\ 0 & 1-\eta & 0 & \eta \end{bmatrix} \begin{bmatrix} x_1 & x_2 & 0 & 0 \\ y_1 & y_2 & 0 & 0 \\ 0 & 0 & x_1 & x_3 \\ 0 & 0 & y_1 & y_3 \end{bmatrix} \begin{bmatrix} \frac{-\phi_2}{\phi_1-\phi_2} \\ \frac{\phi_1}{\phi_1-\phi_2} \\ \frac{-\phi_3}{\phi_1-\phi_3} \\ \frac{\phi_1}{\phi_1-\phi_3} \end{bmatrix} \tag{15}$$

are expressed in terms of the level set function values ϕ_1, ϕ_2 and ϕ_3 at the nodes 1, 2 and 3 respectively of the fixed grid element in which lies the point A, see [69]. In (15), $\{x_1, y_1\}$, $\{x_2, y_2\}$ and $\{x_3, y_3\}$ are coordinates of the points 1, 2 and 3 respectively, while η is the local coordinate of the node in the line segment and is not affected by small variations of the level set at the fixed

[1] If the performance function is a pointwise value, the expression of $F(\tau, \boldsymbol{A}^\star, \boldsymbol{u}^\star)$ will then involve a Dirac function.

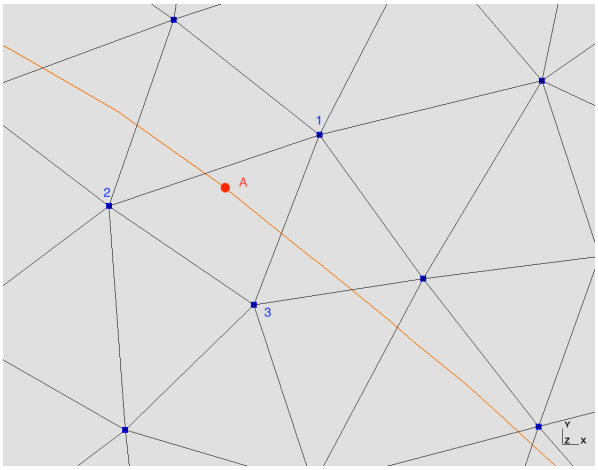

Fig. 10: Superposition of the iso-zero of the level set function and the fixed grid.

grid nodes. Therefore, the sensitivities of the coordinate vector with respect to the nodal values at the nodes of the fixed grid are

$$\frac{\mathrm{d}}{\mathrm{d}\tau}\begin{bmatrix} x \\ y \end{bmatrix} = \begin{bmatrix} 1-\eta & 0 & \eta & 0 \\ 0 & 1-\eta & 0 & \eta \end{bmatrix} \begin{bmatrix} x_1 & x_2 & 0 & 0 \\ y_1 & y_2 & 0 & 0 \\ 0 & 0 & x_1 & x_3 \\ 0 & 0 & y_1 & y_3 \end{bmatrix} \begin{bmatrix} \frac{\phi_2}{(\phi_1-\phi_2)^2} & -\frac{\phi_1}{(\phi_1-\phi_2)^2} & 0 \\ -\frac{\phi_2}{(\phi_1-\phi_2)^2} & \frac{\phi_1}{(\phi_1-\phi_2)^2} & 0 \\ \frac{\phi_3}{(\phi_1-\phi_3)^2} & 0 & -\frac{\phi_1}{(\phi_1-\phi_3)^2} \\ \frac{-\phi_3}{(\phi_1-\phi_3)^2} & 0 & \frac{\phi_1}{(\phi_1-\phi_3)^2} \end{bmatrix} \frac{\mathrm{d}}{\mathrm{d}\tau}\begin{bmatrix} \phi_1 \\ \phi_2 \\ \phi_3 \end{bmatrix} \tag{16}$$

where the level set values are slightly modified for the ill-posed case with a level set equal to zero in all vertices of the element ($\phi_1 = 0$, $\phi_2 = 0$ and $\phi_3 = 0$ simultaneously). This formulae can be extended to 3D case and also to curved interfaces, see [71].

Using the family of mappings (13), the Lie derivative of an arbitrary field ω (scalar field, vector field, or tensor field) in $\Omega(\tau)$ is defined as

$$L_{\mathbf{v}}\omega = \lim_{\delta\tau\to 0} \frac{p_{\delta\tau}^{-1}\omega - \omega}{\delta\tau}, \tag{17}$$

where the index $\mathbf{v}$ in the notation $L_{\mathbf{v}}\omega$ makes reference to the velocity field characterizing the geometrical modification flow.

4.2 Adjoint shape sensitivity of magnetostatics problem

Let us define an augmented Lagrangian function,

$$f_m^a(\tau, \boldsymbol{A}, \boldsymbol{\lambda}_m) = f_m(\tau, \boldsymbol{A}) - r_m(\tau, \boldsymbol{A}, \boldsymbol{\lambda}_m) \tag{18}$$

with $\boldsymbol{\lambda}_m$ a Lagrange multiplier. As (7) implies that the residual $r_m(\tau, \boldsymbol{A}^\star, \boldsymbol{\lambda}_m)$ is zero at equilibrium, one has

$$f_m^a(\tau, \boldsymbol{A}^\star, \boldsymbol{\lambda}_m) = f_m(\tau, \boldsymbol{A}^\star), \tag{19}$$

and the derivative is expressed in terms of f_m^a by

$$\frac{\mathrm{d}f_m}{\mathrm{d}\tau}(\tau, \boldsymbol{A}^\star) = \frac{\mathrm{d}f_m^a}{\mathrm{d}\tau}(\tau, \boldsymbol{A}^\star, \boldsymbol{\lambda}_m). \tag{20}$$

Applying the chain rule, the Lie differentiation of the augmented function (18) with respect to τ yields

$$\frac{\mathrm{d}f_m}{\mathrm{d}\tau} = \int_{\Omega(\tau)} \Big(D_\tau F_m(\tau, \boldsymbol{A}^\star) + \big\{ \mathrm{D}_{\boldsymbol{A}} F_m(\tau, \boldsymbol{A}^\star) \big\} \big(L_{\mathbf{v}} \boldsymbol{A}^\star \big) \\ - L_{\mathbf{v}} (\nu \, \mathbf{curl}\, \boldsymbol{A}^\star) \cdot \mathbf{curl}\, \boldsymbol{\lambda}_m + L_{\mathbf{v}} \boldsymbol{J} \cdot \boldsymbol{\lambda}_m \Big) \, \mathrm{d}\Omega = 0, \tag{21}$$

where we have already omitted the null term. The sensitivity (21) is expressed in terms of the Lie derivative $L_{\mathbf{v}} \boldsymbol{A}^\star$ of the magnetostatics problem (7) solution $\boldsymbol{A}^\star$. The first term in (21) is the partial derivative of the functional,

$$D_\tau F_m(\tau, \boldsymbol{A}^\star) = L_{\mathbf{v}} F_m(\tau, \boldsymbol{A}^\star) \Big|_{L_{\mathbf{v}} \boldsymbol{A} = 0}, \tag{22}$$

whereas the second term is its Fréchet derivative with respect to its field argument,

$$\lim_{|\delta \boldsymbol{A}| \to 0} \frac{1}{|\delta \boldsymbol{A}|} \Big| F_m(\tau, \boldsymbol{A} + \delta \boldsymbol{A}) - F_m(\tau, \boldsymbol{A}) - \big\{ \mathrm{D}_{\boldsymbol{A}} F_m(\tau, \boldsymbol{A}) \big\} \big(\delta \boldsymbol{A} \big) \Big| = 0, \tag{23}$$

where the limit is taken over all sequences of non-zero $\delta \boldsymbol{A}$ that converge to zero. The Fréchet derivative is a linear operator applied to the argument in between parenthesis outside the curly braces, $\mathrm{d}\boldsymbol{A}/\mathrm{d}\tau$, and evaluated in arguments between parenthesis inside the curly braces.

For the current density like $\boldsymbol{J}$, the Lie derivative reads

$$L_{\mathbf{v}} \boldsymbol{J} = \boldsymbol{J} \, \mathrm{div}\, \mathbf{v} - (\nabla \mathbf{v})^{\mathbf{T}} \boldsymbol{J}. \tag{24}$$

Furthermore, a material law like $\boldsymbol{H}(\boldsymbol{B}) = \nu \, \mathbf{curl}\, \boldsymbol{A}$ converts a field quantity, $\boldsymbol{B} = \mathbf{curl}\, \boldsymbol{A}$, into another field quantity, $\boldsymbol{H}$, and contains therefore a geometrical conversion operator, called the Hodge operator, that depends on the metric. Taking into account the implicit Hodge operator when evaluating the Lie derivative of a material law gives,

$$L_{\mathbf{v}} \boldsymbol{H}(\boldsymbol{B}^\star) = \nu^\partial \, \mathbf{curl}\, L_{\mathbf{v}} \boldsymbol{A}^\star + \nu^\partial \Big((\nabla \mathbf{v})^{\mathbf{T}} \boldsymbol{B}^\star - \boldsymbol{B}^\star \, \mathrm{div}\, \mathbf{v} \Big) + (\nabla \mathbf{v}) \, \boldsymbol{H}(\boldsymbol{B}^\star), \tag{25}$$

where

$$\nu^\partial(\boldsymbol{B}) = \nu + \frac{\partial \nu}{\partial \boldsymbol{B}} \boldsymbol{B}$$

is the tangent reluctivity tensor of the material law.

Substituting Eqs. (24) and (25) into (21) yields the linear adjoint system to solve for $\boldsymbol{\lambda}_m$,

$$\int_{\Omega(\tau)} \Big(\big\{ \mathrm{D}_{\boldsymbol{A}} F_m(\tau, \boldsymbol{A}^\star) \big\} \big(L_{\mathbf{v}} \boldsymbol{A}^\star \big) - \nu^\partial \, \mathbf{curl}\, \boldsymbol{\lambda}_m \cdot \mathbf{curl}\, L_{\mathbf{v}} \boldsymbol{A}^\star \Big) \, \mathrm{d}\Omega = 0, \tag{26}$$

for appropriate test function $L_{\mathbf{v}} \boldsymbol{A}^\star$ which, once discretized, has the same system matrix as the tangent stiffness matrix of the problem (7) evaluated for the converged solution $\boldsymbol{A}^\star$ of the nonlinear iterative process. The sensitivity with respect to τ is then given by

$$\frac{\mathrm{d}f_m}{\mathrm{d}\tau}(\tau, \boldsymbol{A}^\star, \boldsymbol{\lambda}_m^\star) = \int_{\Omega(\tau)} \Big(D_\tau F_m(\tau, \boldsymbol{A}^\star) - \nu^\partial \Big((\nabla \mathbf{v})^T \, \mathbf{curl}\, \boldsymbol{A}^\star - \mathbf{curl}\, \boldsymbol{A}^\star \, \mathrm{div}\, \mathbf{v} \Big) \cdot \mathbf{curl}\, \boldsymbol{\lambda}_m^\star \\ - (\nabla \mathbf{v}) \, \nu \, \mathbf{curl}\, \boldsymbol{A}^\star \cdot \mathbf{curl}\, \boldsymbol{\lambda}_m^\star + (\boldsymbol{J} \, \mathrm{div}\, \mathbf{v} - (\nabla \mathbf{v})^T \boldsymbol{J}) \cdot \boldsymbol{\lambda}_m^\star \Big) \, \mathrm{d}\Omega \tag{27}$$

where $\boldsymbol{\lambda}_m^\star$ is the solution of the adjoint problem (26). The rather large number of terms of the sensitivity are advantageously evaluated on a support limited to a one-layer-thick layer of finite elements on both sides of the surfaces involved in the shape variations. The sensitivity calculated analytically is compared with that obtained by finite differences with a perturbation step chosen small enough to avoid truncation and condition errors, see Fig. 11. It observed that the analytic approach matches the finite differences approach with a relative error of 0.01.

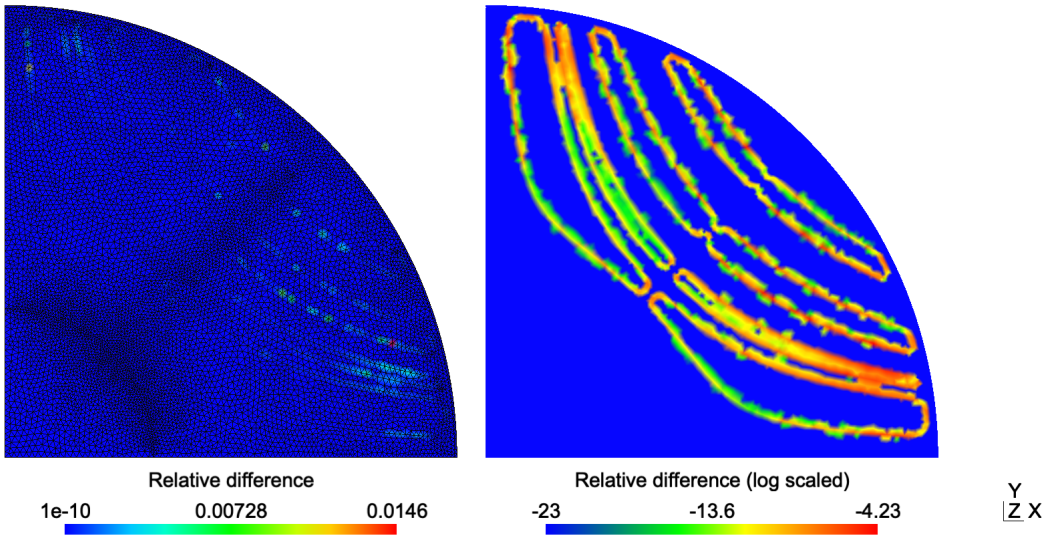

Fig. 11: The relative difference between the sensitivity (27) of the SynRM average torque with respect to the level set field and that calculated by finite differences (left: natural and right: log scaled)

4.3 Adjoint shape sensitivity of linear elastostatic problem

Taking the Lie derivative of an augmented Lagrangian function,

$$f_e^a(\tau, \boldsymbol{u}, \boldsymbol{\lambda}_e) = f_e(\tau, \boldsymbol{u}) - r_e(\tau, \boldsymbol{u}, \boldsymbol{\lambda}_e) \tag{28}$$

with respect to τ yields

$$\begin{aligned} \frac{\mathrm{d}f_e}{\mathrm{d}\tau} = \int_{\Omega(\tau)} \Big(& D_\tau F_e(\tau, \boldsymbol{u}^\star) + \big\{ \mathrm{D}_{\boldsymbol{u}} F_e(\tau, \boldsymbol{u}^\star) \big\} \big(L_{\mathbf{v}} \boldsymbol{u}^\star \big) \\ & - L_{\mathbf{v}} \boldsymbol{\sigma}(\boldsymbol{\epsilon}^\star) : \nabla \boldsymbol{u} + L_{\mathbf{v}} \boldsymbol{g} \cdot \boldsymbol{\lambda}_e \Big) \, \mathrm{d}\Omega, \end{aligned} \tag{29}$$

where $\boldsymbol{\lambda}_e$ is a Lagrange multiplier of (8). The sensitivity (29) is expressed in terms of the Lie derivative $L_{\mathbf{v}} \boldsymbol{u}^\star$ of the linear elasticity problem problem (8) solution $\boldsymbol{u}^\star$. The first term in (29) is the partial derivative of the functional, whereas the second term is its Fréchet derivative with respect to its field argument.

Writing the Hooke tensor as an operator acting on the strain tensor, the Lie derivative of the stress tensor reads, see [44],

$$L_{\mathbf{v}} \boldsymbol{\sigma}(\boldsymbol{\epsilon}) + (\nabla \mathbf{v})^T \boldsymbol{\sigma}(\boldsymbol{\epsilon}) - \boldsymbol{\sigma}(\boldsymbol{\epsilon}) \operatorname{div} \mathbf{v} = \{C\} \big(L_{\mathbf{v}} \nabla \boldsymbol{u} - (\nabla \mathbf{v})(\nabla \boldsymbol{u}) \big), \tag{30}$$

while the Lie derivative of the centrifugal load reads

$$L_{\mathbf{v}} \boldsymbol{g} = -(\nabla \mathbf{v})^{\mathbf{T}} \boldsymbol{g}. \tag{31}$$

Substituting (30) and (31) into (29) yields the linear adjoint system to solve for $\boldsymbol{\lambda}_e$,

$$\int_{\Omega(\tau)} \Big(\big\{ \mathrm{D}_{\boldsymbol{u}} F_e(\tau, \boldsymbol{u}^\star) \big\} \big(L_{\mathbf{v}} \boldsymbol{u}^\star \big) - \{C\} \big(L_{\mathbf{v}} \nabla \boldsymbol{u} \big) : \nabla \boldsymbol{\lambda}_e \Big) \, \mathrm{d}\Omega = 0, \tag{32}$$

which, once discretized, has the same system matrix as the problem (8). The sensitivity with respect to τ is then given by

$$\frac{\mathrm{d}f_e}{\mathrm{d}\tau}(\tau,\boldsymbol{u}^\star) = \int_{\Omega(\tau)} \Big(D_\tau F_e(\tau,\boldsymbol{u}^\star) + \operatorname{div}\mathbf{v}\ \boldsymbol{\sigma}(\boldsymbol{\epsilon}^\star) : \nabla\boldsymbol{\lambda}_e - \boldsymbol{\sigma}\big((\nabla\mathbf{v})(\nabla\boldsymbol{u}^\star)\big) : \nabla\boldsymbol{\lambda}_e \\ - \boldsymbol{\sigma}(\boldsymbol{\epsilon}^\star) : \big((\nabla\mathbf{v})(\nabla\boldsymbol{\lambda}_e)\big) \Big)\ \mathrm{d}\Omega, \tag{33}$$

where $\boldsymbol{\lambda}_e^\star$ is the solution of the adjoint problem (32). The rather large number of terms of the sensitivity are again evaluated on a support limited to a one-layer-thick layer of finite elements on both sides of the surfaces involved in the shape variations.

5 Application to the electro-mechanical design of a SynRM

Let us perform a level set topology optimisation design to the SynRM rotor in order to smoothen the von Mises stress criterion in steel parts while keeping the average torque and torque ripples respectively to acceptable levels. The topology optimisation problem (9) reads:

$$\begin{aligned} \min_{\tau} \quad & f_0(\tau,\boldsymbol{A}^\star,\boldsymbol{u}^\star) \equiv \sigma_{PN} \\ s.t. \quad & f_1(\tau,\boldsymbol{A}^\star,\boldsymbol{u}^\star) \equiv \frac{1}{N_p}\sum_{R=1}^{N_p} T_R - T^\star \geq 0, \\ & f_2(\tau,\boldsymbol{A}^\star,\boldsymbol{u}^\star) \equiv \big(T_R/T^\star - 1\big)^2 - T_\epsilon^2 \leq 0,\ R=1,\ldots,N_p, \\ & -1 \leq \tau \leq 1 \\ & r_m(\tau,\boldsymbol{A}^\star,\bar{\boldsymbol{A}}) = 0,\ \forall\bar{\boldsymbol{A}} \\ & r_e(\tau,\boldsymbol{u}^\star,\bar{\boldsymbol{u}}) = 0,\ \forall\bar{\boldsymbol{u}}, \end{aligned} \tag{34}$$

For the optimisation at hand, (34), the electromagnetic performance of the machine is evaluated under a quasi-static assumption. The stator windings are thus supplied with the prescribed three-phase currents (nominal value of 217 A) and the simulation is done for a series of $N_p = 8$ equidistant rotor positions over one angular torque period (ranging from 0 to 7.5 degrees) as a succession of static computations. The electromagnetic symmetries are also exploited to simulate only a quarter of the machine by means of appropriate periodicity boundary conditions. The nonlinear finite element model takes the anhysteretic saturation curve of a M400-50A steel grade (see Fig. 12), and it is solved by means of a Newton-Raphson method.

A method based on Maxwell's stress tensor is used for the computation of torque. Choosing a circular shell of axial length L_a and surface S_a in the air gap, denoted Ω_g, of the machine as a closed integration surface that surrounds the rotor, the torque at a given rotor position θ_R reads,

$$T_R = \int_{\Omega_g} \nu_0\ t_g\ B_r\ B_\theta\ \mathrm{d}\Omega, \tag{35}$$

with

$$t_g = 2\pi\frac{L_a}{S_a}\boldsymbol{r}\cdot\boldsymbol{r} \tag{36}$$

being a geometrical coefficient where $\boldsymbol{r}$ is the radial vector, $B_r = \boldsymbol{B}^\star\cdot\boldsymbol{e}_r$ and $B_\theta = \boldsymbol{B}^\star\cdot\boldsymbol{e}_\theta$ are the scalar product of $\boldsymbol{B}^\star$ with respectively the radial basis vector $\boldsymbol{e}_r$ and tangential basis vector $\boldsymbol{e}_\theta$.

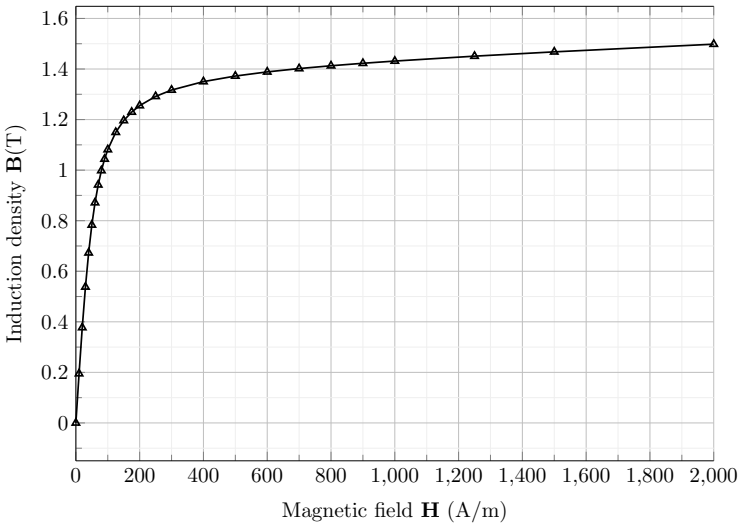

Fig. 12: Magnetization curve of the laminated steel M400-50A.

The electromagnetic design is followed by a proper mechanical design based on a linear elastic constitutive behaviour with a Young's modulus of 210 (MPa), a Poisson ratio of 0.3 and a density of 7.7 (g/cm^3). The rotor is subjected to the centrifugal body load with a rotating speed of 4800 RPMs around its axis. In order to speed up the design process, an accurate fatigue life assessment is not performed, but we rather limit ourselves to the maximum speed. The local von Mises stress criterion σ_e is aggregated into a single functional in the steel parts (Ω_1) by means of the L^p-norm, [25],

$$\sigma_{PN} = \Big(\int_{\Omega_1} \sigma_e^p \ \mathrm{d}\Omega \Big)^{1/p}, \tag{37}$$

where p is the L^p-norm parameter.

The evaluation of the performance functions f_0 and f_j, $j = 1, 2$ for a given level set distribution, τ, is performed by solving the nonlinear magnetostatic problem (7) at N_p rotor positions using a mesh conformal to the boundaries of the level set and evaluating the torque T_R at each position θ_R by making use of (35). It also requires solving the linear elastic problem in the steel (solid) parts only, at a single rotor position and evaluating the L^p-norm of the von Mises stress (37).

The computational chain is based on Gmsh [32] for the mesh generation and sparselizard [35] for the nonlinear magnetostatic computation. Furthermore, two in-house software packages are considered: on the one hand, Morfeo [2], which is a thermo-mechanical finite element software with topology optimisation capabilities, and, on the other hand, MadLIB, which is a library for advanced mesh adaptations. The optimisation problem (34) is solved by the MMA [61] algorithm which makes use of the sensitivity formulas (27) and (33) derived so far. In what follows, $T^\star$ (the target value for the average torque) set to 1100 Nm with 10% ripples ($T_\epsilon = 5\%$). For the mechanical part, the von Mises stresses should be less than (or equal to) 75% of the elastic limit at maximum speed (350 MPa).

The successive iterations of the optimisation algorithm are summarized in Fig. 13. While the design domain (level set) is advantageously discretized in a fixed grid using $23,470$ triangular elements and filtering a set of nodal optimisation variables at each point by means of a Helmholtz type filter [47], the analysis domain is discretized by means of a body-fitted mesh using on average

32, 321 triangular elements at each iteration. Starting with the design domain initially seeded with holes, the optimisation results, after roughly 165 iterations, in a rotor with two flux-barriers and a number of radial ribs determined automatically in each flux-barrier. The complexity of the holes (flux-barriers) pattern requires a rather fine mesh for the accurate FEM analysis. The design shows the ability of the method to recover similar layouts to those obtained by imposing design rules as in [8] or [12].

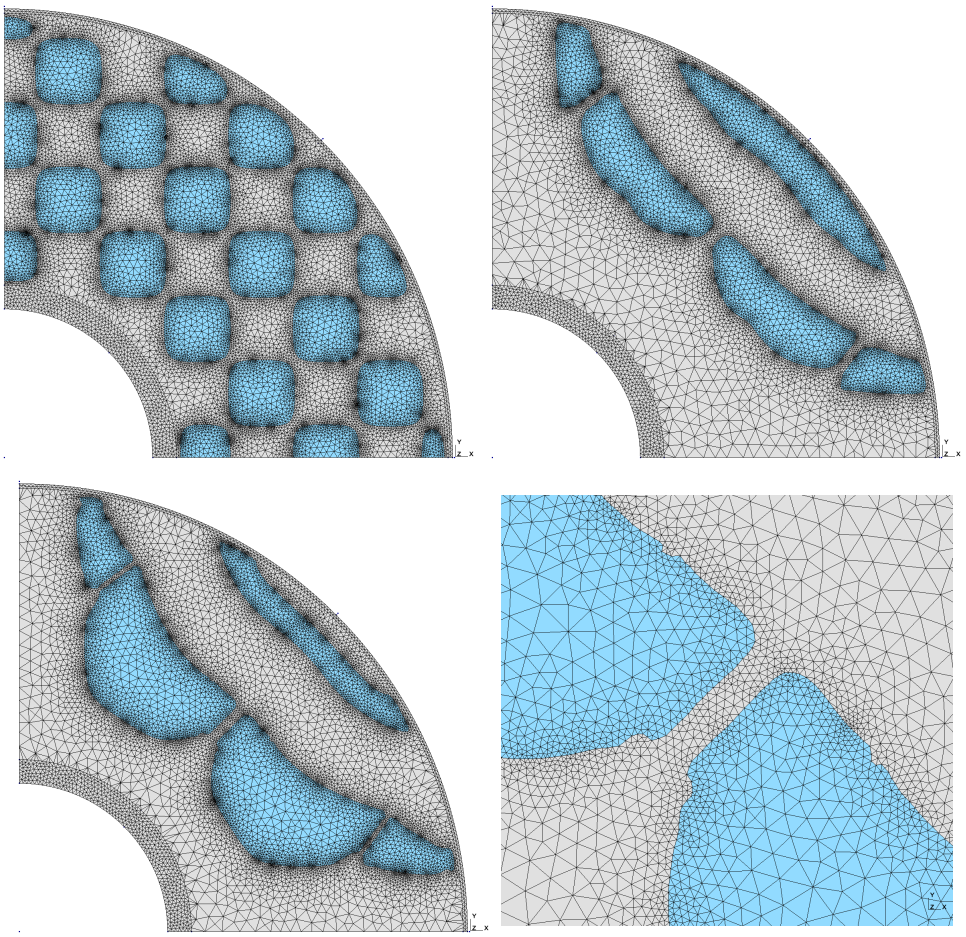

Fig. 13: The rotor of the SynRM with the initial hole seeding (top left) is optimised successfully until meeting both the torque requirements and the mechanical feasibility. The mesh conformal to the level set boundaries is shown after 20 iterations (top right) and at the last iteration (bottom).

To further investigate the influence of the initial seeding, the optimization problem is solved starting from a design with a lowered number of holes and using the same refinement level for the body-fitted mesh. As expected, the results gathered in Fig. 14 show that the design is sensitive to the initial seeding. While the rotor still has two flux barriers, there is now only one radial rib on the largest barrier. While keeping a constant level of body-fitted mesh refinement, it appears that more holes in the initial design allow the creation of finer structures during optimisation.

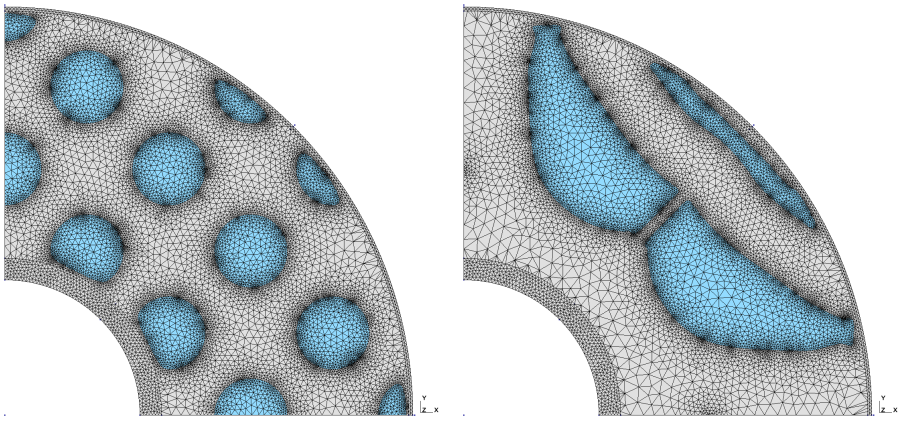

Fig. 14: The optimisation of the SynRM rotor with the modified initial hole seeding (left) results in a rotor with two flux barriers (right) where only one of which has a single radial rib.

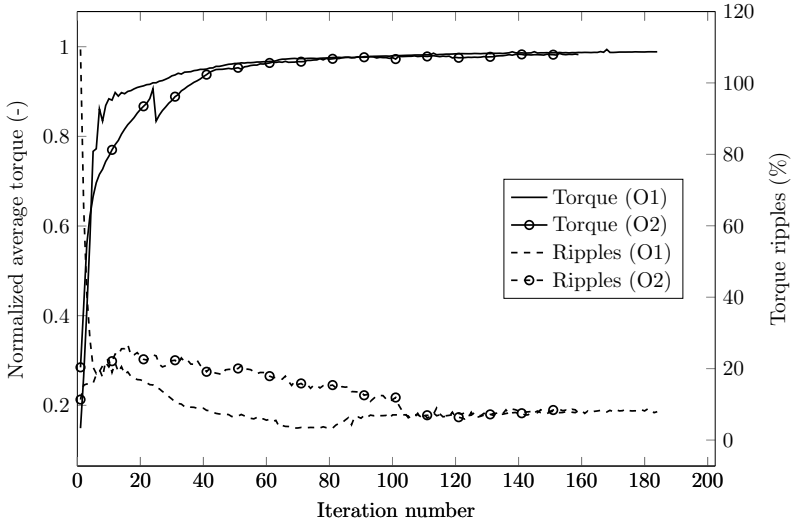

Fig. 15: Convergence of the normalized average torque and ripples to the desired values for the optimisation started with two different configurations (O1: configuration of Fig. 13; and O2: configuration of Fig 14.

Although the optimizations resulted in different designs, both of them exhibit the same levels of average torque with less than 10% torque ripples, Fig. 15, both meeting hence the expected requirements. The differences lie mainly in the level of von Mises stress along the radial bridges, as well as in the displacement of the outer ring, see Fig. 16, the stress levels everywhere else in the rotor are below the maximum stress criterion. The optimised design obtained with the lowered number of holes in the initial seeding exhibits the lowest level of von Mises stress and displacement.

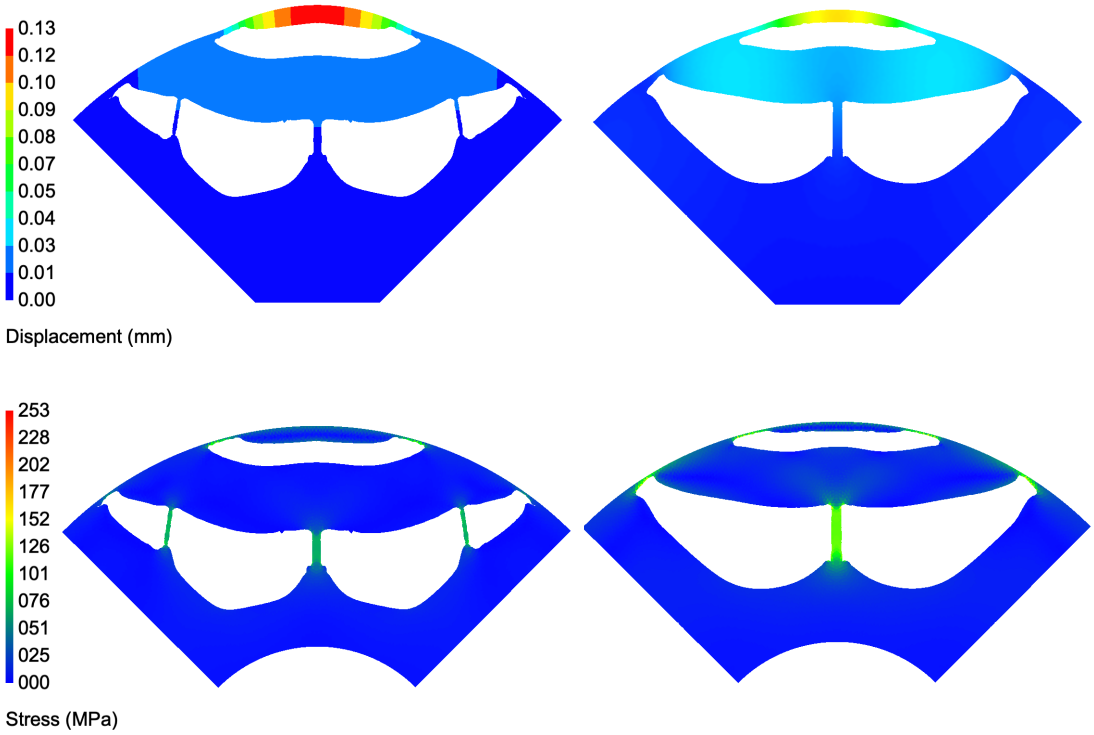

Fig. 16: The displacement (magnified with a factor 50), top, and the level of von Mises stress criterion, bottom, for the designs of Fig. 13 (left colum) and Fig 14, respectively.

6 Conclusions and perspectives

We have developed a mathematical framework for handling accurately the complex topological modifications which occur through topology optimisation based on a level set method. The domains delineated by the level set function are discretised by conformal meshes in order to enable accurate FEM analyses. Following the general framework of shape sensitivity analysis, we can obtain the sensitivity with respect to the shape modifications. The theoretical results gathered in the article have been successfully applied to electro-mechanical optimisation of the topology of energy conversion system which is of a great importance in automotive applications. Our optimisation process delivered a valid design, achieving the expected torque levels for the given supply conditions, and ensuring structural integrity regarding centrifugal forces.

Replication of results

Our work relies on several programming languages (Python, C++) and also several other codes. Specifically, we use the described topology optimisation with body-fitted mesh representation based on the in-house software Morfeo [2]. The mesh adaptations are performed with MadLIB [1] and the nonlinear magnetostatics is solved with Sparselizard [35]. Rather than providing a source code package which would only work under very strict platform requirements, we instead opt to

aid the reader in reproducing our results by satisfying the reasonable and responsible demands for the open source codes underpinning the present article.

Acknowledgements The first author warmly thanks Dr. Alexandre Halbach for his support with sparselizard.

Conflict of interest

On behalf of all authors, the corresponding author states that there is no conflict of interest.

References

1. Madlib: Mesh adaptation library, Cenaero, Belgium. Web page: `https://sites.uclouvain.be/madlib/`
2. Morfeo version 3.1.0 (2019), a Manufacturing ORiented Finite Element sOftware, Cenaero, Belgium. Web page: `http://www.cenaero.be`
3. Abe, K., Kazama, S., Koro, K.: A boundary element approach for topology optimization problem using the level set method. Communications in numerical methods in engineering **23**(5), 405–416 (2007)
4. Alauzet, F.: Size gradation control of anisotropic meshes. Finite Elements in Analysis and Design **46**(1-2), 181–202 (2010)
5. Allaire, G., Dapogny, C., Frey, P.: A mesh evolution algorithm based on the level set method for geometry and topology optimization. Structural and Multidisciplinary Optimization **48**(4), 711–715 (2013)
6. Allaire, G., Dapogny, C., Frey, P.: Shape optimization with a level set based mesh evolution method. Computer Methods in Applied Mechanics and Engineering **282**, 22–53 (2014)
7. Allaire, G., Jouve, F., Toader, A.M.: A level-set method for shape optimization. Comptes Rendus Mathematique **334**(12), 1125–1130 (2002)
8. Barcaro, M., Meneghetti, G., Bianchi, N.: Structural analysis of the interior pm rotor considering both static and fatigue loading. IEEE Transactions on Industry Applications **50**(1), 253–260 (2013)
9. Bendsøe, M.P., Kikuchi, N.: Generating optimal topologies in structural design using a homogenization method. Computer methods in applied mechanics and engineering **71**(2), 197–224 (1988)
10. Bendsoe, M.P., Sigmund, O.: Topology optimization: theory, methods, and applications. Springer Science & Business Media (2003)
11. Biedinger, J., Lemoine, D.: Shape sensitivity analysis of magnetic forces. Magnetics, IEEE Transactions on **33**(3), 2309–2316 (1997)
12. Binder, A., Schneider, T., Klohr, M.: Fixation of buried and surface-mounted magnets in high-speed permanent-magnet synchronous machines. IEEE Transactions on Industry Applications **42**(4), 1031–1037 (2006)
13. Boglietti, A., Cavagnino, A., Pastorelli, M., Staton, D., Vagati, A.: Thermal analysis of induction and synchronous reluctance motors. IEEE Transactions on Industry Applications **42**(3), 675–680 (2006)
14. Bossavit, A.: Computational electromagnetism: variational formulations, complementarity, edge elements. Academic Press (1998)
15. Braibant, V., Fleury, C.: Shape optimal design using b-splines. Computer Methods in Applied Mechanics and Engineering **44**(3), 247–267 (1984)
16. Chai, F., Li, Y., Liang, P., Pei, Y.: Calculation of the maximum mechanical stress on the rotor of interior permanent-magnet synchronous motors. IEEE Transactions on Industrial Electronics **63**(6), 3420–3432 (2016)
17. Choi, K.K., Chang, K.H.: A study of design velocity field computation for shape optimal design. Finite Elem. Anal. Des. **15**(4), 317–341 (1994)
18. Credo, A., Fabri, G., Villani, M., Popescu, M.: Adopting the topology optimization in the design of high-speed synchronous reluctance motors for electric vehicles. IEEE Transactions on Industry Applications **56**(5), 5429–5438 (2020)
19. Dapogny C, D.C., P, F.: Three-dimensional adaptive domain remeshing, implicit domain meshing, and applications to free and moving boundary problems. Journal of Computational Physics **262**, 358–378 (2014)
20. Deaton, J.D., Grandhi, R.V.: A survey of structural and multidisciplinary continuum topology optimization: post 2000. Structural and Multidisciplinary Optimization **49**(1), 1–38 (2014)
21. Di Nardo, M., Calzo, G.L., Galea, M., Gerada, C.: Design optimization of a high-speed synchronous reluctance machine. IEEE Transactions on Industry Applications **54**(1), 233–243 (2017)
22. Di Nardo, M., Galea, M., Gerada, C., Palmieri, M., Cupertino, F.: Multi-physics optimization strategies for high speed synchronous reluctance machines. In: 2015 IEEE Energy Conversion Congress and Exposition (ECCE), pp. 2813–2820. IEEE (2015)

23. Di Nardo, M., Galea, M., Gerada, C., Palmieri, M., Cupertino, F., Mebarki, S.: Comparison of multi-physics optimization methods for high speed synchrnous reluctance machines. In: IECON 2015-41st Annual Conference of the IEEE Industrial Electronics Society, pp. 002771–002776. IEEE (2015)
24. van Dijk, N.P., Maute, K., Langelaar, M., Van Keulen, F.: Level-set methods for structural topology optimization: a review. Structural and Multidisciplinary Optimization **48**(3), 437–472 (2013)
25. Duysinx, P., Sigmund, O.: New developments in handling stress constraints in optimal material distribution. Proceedings of the 7th AIAA/USAF/NASAISSMO Symp on Multidisciplinary Analysis and Optimization **1**, 1501–1509 (1998)
26. Emmendoerfer Jr, H., Fancello, E.A.: Topology optimization with local stress constraint based on level set evolution via reaction–diffusion. Computer Methods in Applied Mechanics and Engineering **305**, 62–88 (2016)
27. Feppon, F., Allaire, G., Bordeu, F., Cortial, J., Dapogny, C.: Shape optimization of a coupled thermal fluid–structure problem in a level set mesh evolution framework. SeMA Journal **76**(3), 413–458 (2019)
28. Florez S Shakoor M, T.T., M, B.: A new finite element strategy to simulate microstructural evolutions. Computational Material Science **172** (2020)
29. Fratta, A., Toglia, G., Vagati, A., Villata, F.: Ripple evaluation of high-performance synchronous reluctance machines. IEEE Industry applications magazine **1**(4), 14–22 (1995)
30. Gangl, P., Langer, U., Laurain, A., Meftahi, H., Sturm, K.: Shape optimization of an electric motor subject to nonlinear magnetostatics. SIAM Journal on Scientific Computing **37**(6), B1002–B1025 (2015)
31. Geiss, M.J., Boddeti, N., Weeger, O., Maute, K., Dunn, M.L.: Combined level-set-xfem-density topology optimization of four-dimensional printed structures undergoing large deformation. Journal of Mechanical Design **141**(5) (2019)
32. Geuzaine, C., Remacle, J.F.: Gmsh: A 3-D finite element mesh generator with built-in pre-and post-processing facilities. International Journal for Numerical Methods in Engineering **79**(11), 1309–1331 (2009)
33. Gilmanov, A., Sotiropoulos, F.: A hybrid cartesian/immersed boundary method for simulating flows with 3d, geometrically complex, moving bodies. Journal of computational physics **207**(2), 457–492 (2005)
34. Ha, S.H., Cho, S.: Level set based topological shape optimization of geometrically nonlinear structures using unstructured mesh. Computers & structures **86**(13-14), 1447–1455 (2008)
35. Halbach, A.: Sparselizard-the user friendly finite element c++ library: `http://www.cenaero.be` (2017)
36. Hassani, B., Tavakkoli, S.M., Ghasemnejad, H.: Simultaneous shape and topology optimization of shell structures. Structural and Multidisciplinary Optimization **48**(1), 221–233 (2013)
37. Henrotte, F.: Handbook for the computation of electromagnetic forces in a continuous medium. Int. Compumag Society Newsletter **24**(2), 3–9 (2004)
38. Hermann, R., et al.: Harley flanders, differential forms with applications to the physical sciences. Bulletin of the American Mathematical Society **70**(4), 483–487 (1964)
39. Hintermüller, M., Laurain, A.: Electrical impedance tomography: from topology to shape. Control & Cybernetics **37**(4) (2008)
40. Hiptmair, R., Li, J.: Shape derivatives in differential forms i: An intrinsic perspective. Annali di Matematica Pura ed Applicata **192**(6), 1077–1098 (2013)
41. Hiptmair, R., Li, J.: Shape derivatives in differential forms ii: Shape derivatives for scattering problems. SAM Seminar for Applied Mathematics, ETH, Zürich, Switzerland, Research Report (2017)
42. Jansen, M.: Explicit level set and density methods for topology optimization with equivalent minimum length scale constraints. Structural and Multidisciplinary Optimization **59**(5), 1775–1788 (2019)
43. Kostko, J.: Polyphase reaction synchronous motors. Journal of the American Institute of Electrical Engineers **42**(11), 1162–1168 (1923)
44. Kuci, E., Henrotte, F., Duysinx, P., Geuzaine, C.: Design sensitivity analysis for shape optimization based on the Lie derivative. Computer Methods in Applied Mechanics and Engineering **317**, 702 – 722 (2017)
45. Kuci, E., Henrotte, F., Geuzaine, C., Dehez, B., Gref, C.D., Versle, C., Friebel, C.: Design Optimization of Synchronous Reluctance Machines for Railway Traction Application Including Assembly Process Constraints. In: 2020 International Conference on Electrical Machines (ICEM), vol. 1, pp. 117–123 (2020). DOI 10.1109/ICEM49940.2020.9270859. ISSN: 2381-4802
46. Kwack, J., Min, S., Hong, J.P.: Optimal stator design of interior permanent magnet motor to reduce torque ripple using the level set method. IEEE Transactions on Magnetics **46**(6), 2108–2111 (2010)
47. Lazarov, B.S., Sigmund, O.: Filters in topology optimization based on helmholtz-type differential equations. International Journal for Numerical Methods in Engineering **86**(6), 765–781 (2011)
48. Le, C., Bruns, T., Tortorelli, D.: A gradient-based, parameter-free approach to shape optimization. Computer Methods in Applied Mechanics and Engineering **200**(9-12), 985–996 (2011)
49. Lindh, P., Tehrani, M.G., Lindh, T., Montonen, J.H., Pyrhönen, J., Sopanen, J.T., Niemelä, M., Alexandrova, Y., Immonen, P., Aarniovuori, L., et al.: Multidisciplinary design of a permanent-magnet traction motor for a hybrid bus taking the load cycle into account. IEEE Transactions on Industrial Electronics **63**(6), 3397–3408 (2016)
50. Moës, N., Dolbow, J., Belytschko, T.: A finite element method for crack growth without remeshing. International journal for numerical methods in engineering **46**(1), 131–150 (1999)

51. Noël, L., Miegroet, L.V., Duysinx, P.: Analytical sensitivity analysis using the extended finite element method in shape optimization of bimaterial structures. International Journal for Numerical Methods in Engineering **107**(8), 669–695 (2016)
52. Novotny, A.A., Feijóo, R.A., Taroco, E., Padra, C.: Topological sensitivity analysis. Computer methods in applied mechanics and engineering **192**(7), 803–829 (2003)
53. Olhoff, N., Bendsøe, M.P., Rasmussen, J.: On cad-integrated structural topology and design optimization. Computer Methods in Applied Mechanics and Engineering **89**(1-3), 259–279 (1991)
54. Osher, S., Sethian, J.A.: Fronts propagating with curvature-dependent speed: algorithms based on hamilton-jacobi formulations. Journal of computational physics **79**(1), 12–49 (1988)
55. Palmieri, M., Perta, M., Cupertino, F.: Design of a 50.000-r/min synchronous reluctance machine for an aeronautic diesel engine compressor. IEEE Transactions on Industry Applications **52**(5), 3831–3838 (2016)
56. Park, I.H., Coulomb, J.L., Hahn, S.Y.: Implementation of continuum sensitivity analysis with existing finite element code. Magnetics, IEEE Transactions on **29**(2), 1787–1790 (1993)
57. Sigmund, O., Maute, K.: Topology optimization approaches. Structural and Multidisciplinary Optimization **48**(6), 1031–1055 (2013)
58. Sokolowski, J., Zochowski, A.: Optimality conditions for simultaneous topology and shape optimization. SIAM journal on control and optimization **42**(4), 1198–1221 (2003)
59. Sokolowski, J., Zolesio, J.P.: Introduction to shape optimization. In: Introduction to Shape Optimization, pp. 5–12. Springer (1992)
60. Svanberg, K.: The method of moving asymptotes- a new method for structural optimization. International journal for numerical methods in engineering **24**(2), 359–373 (1987)
61. Svanberg, K.: A class of globally convergent optimization methods based on conservative convex separable approximations. SIAM Journal on Optimization pp. 555–573 (2002)
62. Tanaka, I., Nitomi, H., Imanishi, K., Okamura, K., Yashiki, H.: Application of high-strength nonoriented electrical steel to interior permanent magnet synchronous motor. IEEE Transactions on Magnetics **49**(6), 2997–3001 (2012)
63. Tseng, Y.H., Ferziger, J.H.: A ghost-cell immersed boundary method for flow in complex geometry. Journal of computational physics **192**(2), 593–623 (2003)
64. Van Miegroet, L., Duysinx, P.: Stress concentration minimization of 2d filets using x-fem and level set description. Structural and Multidisciplinary Optimization **33**(4), 425–438 (2007)
65. Villanueva, C.H., Maute, K.: Cutfem topology optimization of 3d laminar incompressible flow problems. Computer Methods in Applied Mechanics and Engineering **320**, 444–473 (2017)
66. Wang, M.Y., Wang, X., Guo, D.: A level set method for structural topology optimization. Computer methods in applied mechanics and engineering **192**(1), 227–246 (2003)
67. Yaji, K., Otomori, M., Yamada, T., Izui, K., Nishiwaki, S., Pironneau, O.: Shape and topology optimization based on the convected level set method. Structural and Multidisciplinary Optimization **54**(3), 659–672 (2016)
68. Yamasaki, S., Kawamoto, A., Nomura, T.: Compliant mechanism design based on the level set and arbitrary lagrangian eulerian methods. Structural and Multidisciplinary Optimization **46**(3), 343–354 (2012)
69. Yamasaki, S., Kawamoto, A., Nomura, T., Fujita, K.: A consistent grayscale-free topology optimization method using the level-set method and zero-level boundary tracking mesh. International Journal for Numerical Methods in Engineering **101**(10), 744–773 (2015)
70. Yamasaki, S., Nomura, T., Kawamoto, A., Sato, K., Nishiwaki, S.: A level set-based topology optimization method targeting metallic waveguide design problems. International Journal for Numerical Methods in Engineering **87**(9), 844–868 (2011)
71. Yamasaki, S., Yamanaka, S., Fujita, K.: Three-dimensional grayscale-free topology optimization using a level-set based r-refinement method. International Journal for Numerical Methods in Engineering **112**(10), 1402–1438 (2017)
72. Zhang, J., Zhang, W., Zhu, J., Xia, L.: Integrated layout design of multi-component systems using xfem and analytical sensitivity analysis. Computer Methods in Applied Mechanics and Engineering **245**, 75–89 (2012)
73. Zienkiewicz, C., Taylor, R.L.: The finite element method Vol. 1: Basic formulation and linear problems. No. 3 in finite element method series. Wiley (1990)